Electronic Supplementary Material (ESI) for Physical Chemistry Chemical Physics.
This journal is © the Owner Societies 2021

Supplementary Material

Thermoelectric properties of CZTS thin films: effect of Cu-Zn disorder

E. Isotta[1,*], U. Syafiq[1,2,*], N. Ataollahi[1], A. Chiappini[3], C. Malerba[4], S. Luong[5], V. Trifiletti[5], O. Fenwick[5], N.M. Pugno[1,5,6], and P. Scardi[1,*]

[1]*Department of Civil, Environmental and Mechanical Engineering, University of Trento, Trento, Italy*
[2]*Solar Energy Research Institute, National University of Malaysia (SERI-UKM), 43600 Bangi, Selangor, Malaysia*
[3]*IFN-CNR CSMFO Lab. and FBK Photonics Unit, Trento, Italy.*
[4]*Italian National Agency for New Technologies, Energy and Sustainable Economic Development (ENEA), Rome, Italy*
[5]*School of Engineering and Materials Science, Queen Mary University of London, London, United Kingdom*
[6]*Laboratory of Bio-inspired, Bionic, Nano, Meta Materials & Mechanics, Department of Civil, Environmental and Mechanical Engineering, University of Trento, Trento, Italy*

Supplementary Note 1: Synthesis of CZTS nanoparticle ink

As described in the main text, CZTS nanoparticle inks were prepared according to the method described by Syafiq et al.[1], with a modified setup for N_2 and vacuum lines as shown in Figure S1.

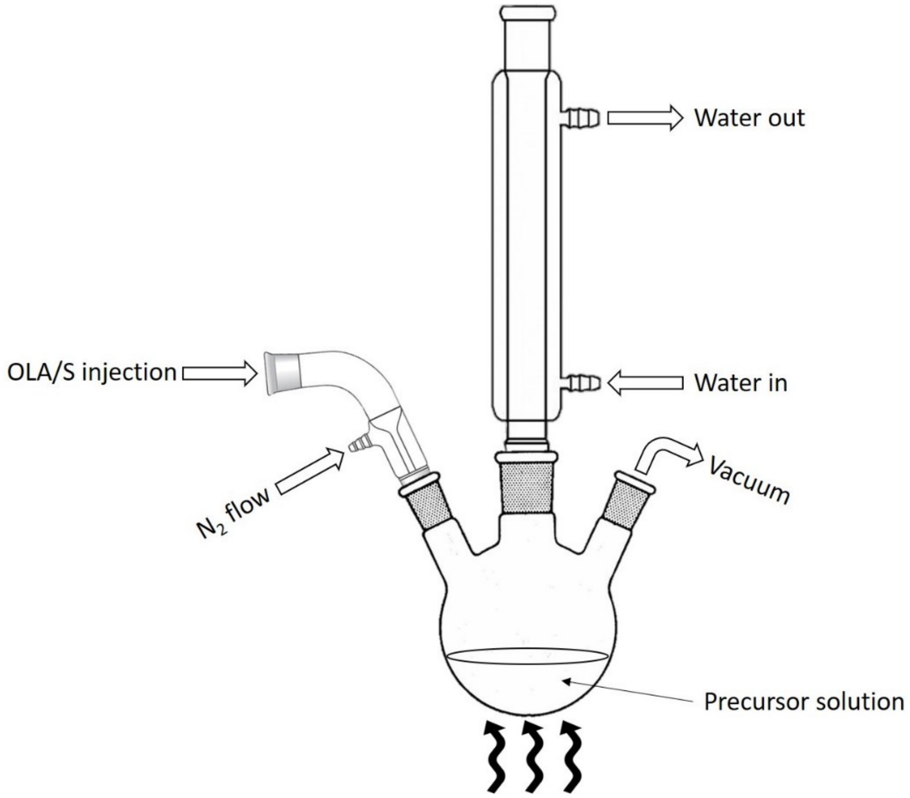

Figure S1. Modified setup for CZTS nanoparticles ink synthesis.

Supplementary Note 2: Raman spectra without background correction

Raman spectra without background correction are visible in Figure S2. They have been collected for the slowly cooled and quenched samples using 532nm and 785 nm laser excitation sources. A fit of the spectra was performed with the software PM2K[2], using a set of nine Lorentzian peaks.

As commented in the main text, for the 785 nm excitation source and quenched sample, Raman modes appear of very modest intensity upon a sloped background that we associate to photoluminescence effects. A similar effect on the spectrum has been reported by other groups as well.[3]

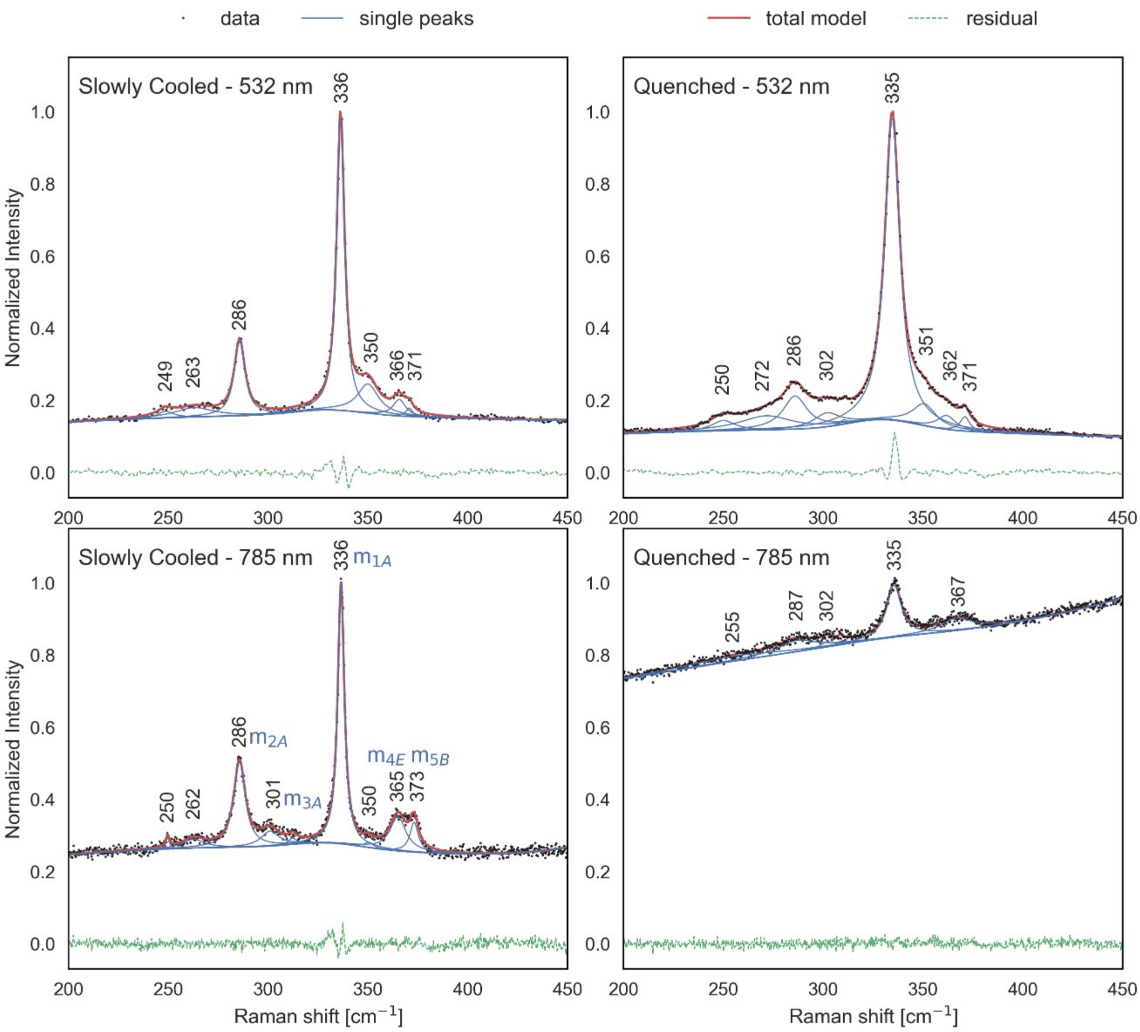

Figure S2. Near-resonant Raman spectroscopy and peak fitting using Lorentzian curves. A sample slowly cooled after the thermal treatment and another quenched from a 350°C post-annealing are shown, both measured with excitation wavelengths of 532 nm and 785 nm. Intensities are normalized with respect to the main mode. Mode labelling can be seen in the lower left quadrant.

Supplementary Note 3: UV-Vis spectroscopy

Figure S3 shows the Tauc’s plot obtained from the UV-Vis spectra for a slowly cooled and a quenched spin-coated sample. The bandgap was extrapolated using the formula $ahv = A(hv - Eg)^{1/2}$, where a is the absorption coefficient, h is the Planck’s constant, ν is the light frequency, A is the transition constant and Eg is the bandgap. As visible, the quenched sample presents a lower bandgap, attributed to the larger presence of kesterite in the tetragonal disordered form (*I-42m*). This is considered the reason for the reduction of Raman signal at 785 nm. Indeed, the bandgap gets smaller with respect to the excitation wavelength (785 nm = 1.58 eV) thus moving the system away from resonance conditions.

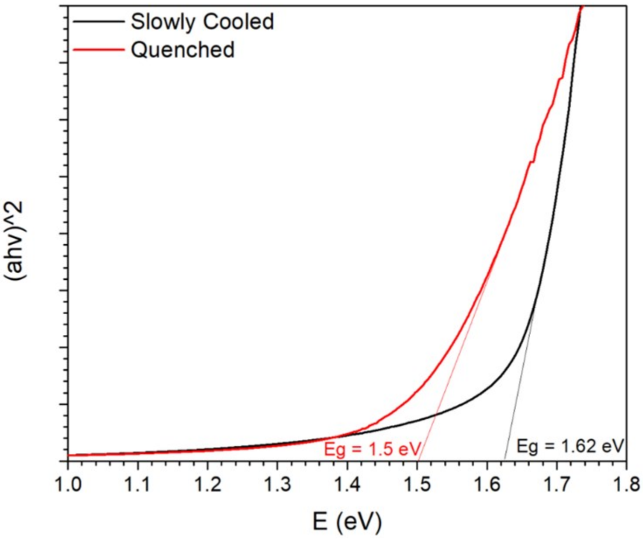

Figure S3. Tauc plot from UV-Vis spectroscopy for a slowly cooled and a quenched sample made with spin coating. Extrapolation of the bandgap is visible.

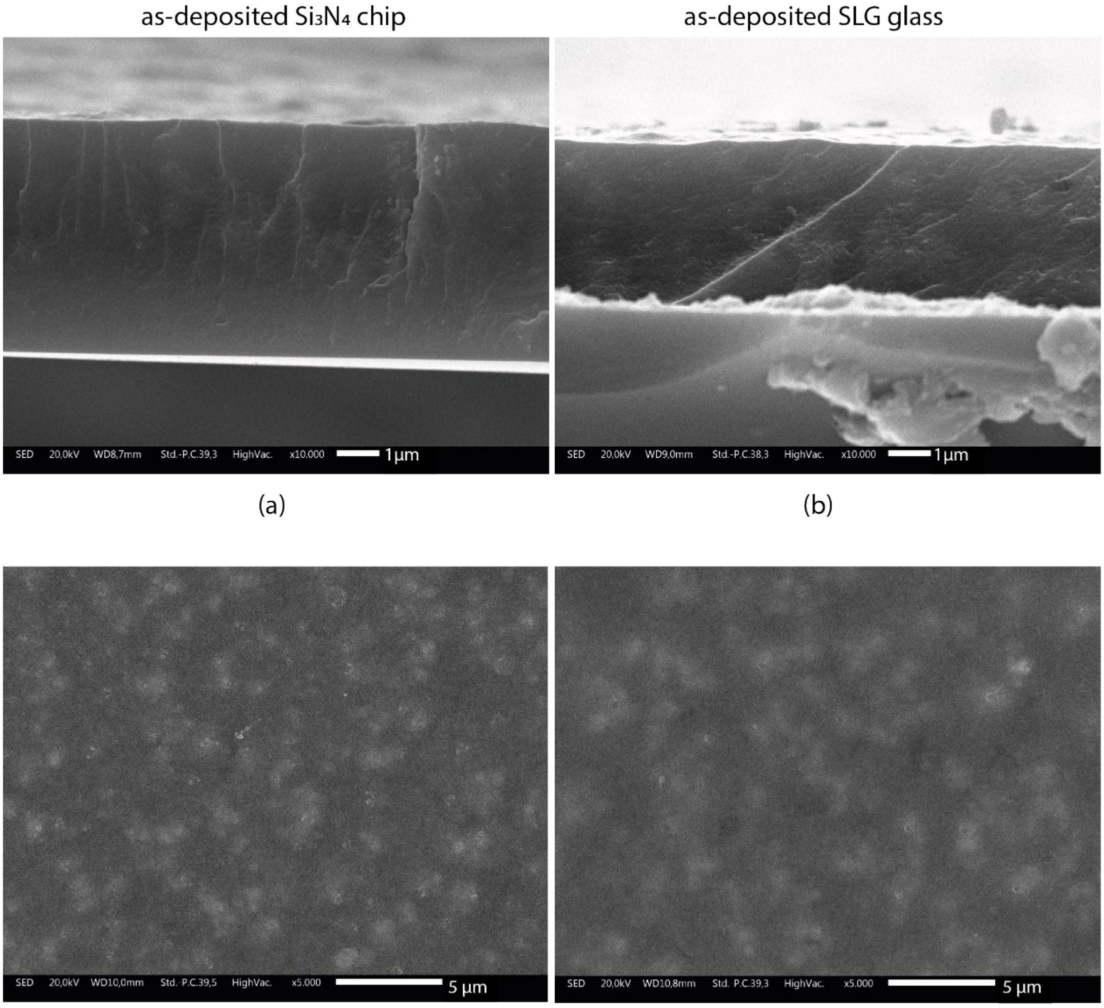

(a) (b)

(c) (d)

Figure S4: SEM images for as-deposited samples, deposited respectively on measurement Si_3N_4 chips (a,c) and on SLG substrates (b,d). Pictures (a,b) show fracture surfaces while pictures (c,d) show top-views of the samples.

Supplementary Note 4: further SEM images

Supplementary Note 5: Density measurements

Geometrical measurements of density were performed on some thermally treated spin coated samples. The mass of the film was measured by the difference in weight before and after scratching it away from the substrate. Large-area samples (>25mm*25mm) were used. Measured weights were around three orders of magnitude higher than the sensitivity of the scale. Thicknesses were measured with a profilometer. The average sample density is ~98%, with the lowest measured value of 93%.

Figure S5 shows additional SEM images on a polished sample (a) and magnified fracture surface of an as-deposited sample (b). Given the low resolution, it is not possible to reliably quantify porosity. Nevertheless, the films look compact and pin-hole free, thus being compatible with the geometrical measurements of density.

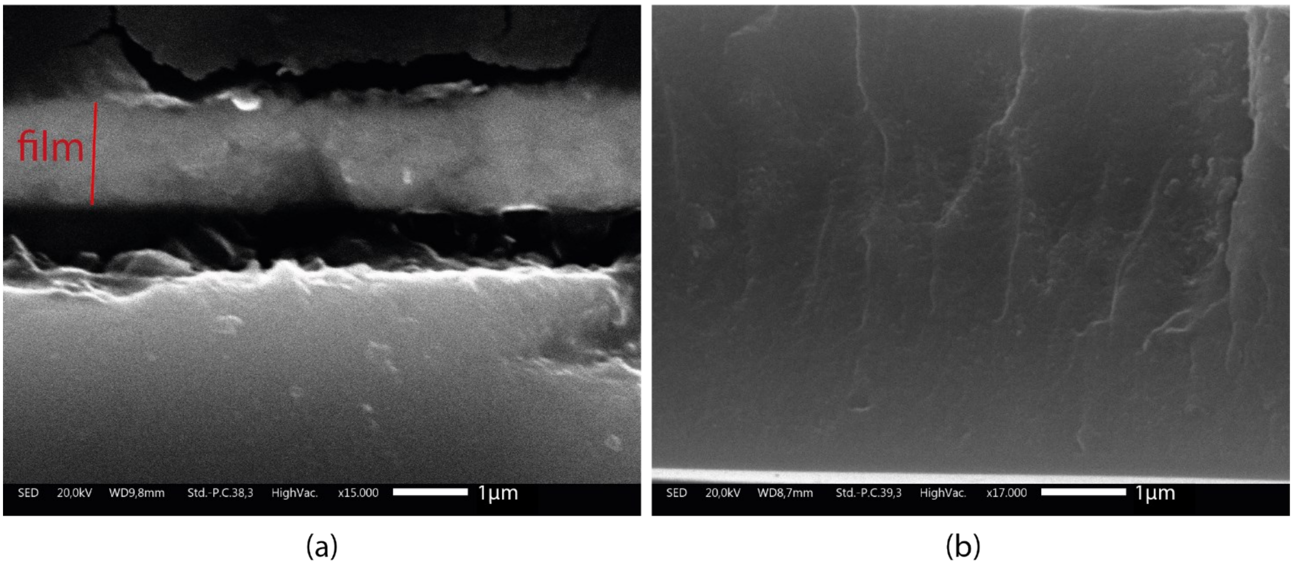

(a) (b)

Figure S5: SEM images for *a polished spin-coated and thermally-treated sample, incorporated in resin (a), and magnified fracture surface of an as-deposited spin coated sample (b).*

Supplementary Note 6: Estimation of thermal conductivity and figure of merit for thermally treated samples

The thermal conductivity k for the thin film spin coated sample has been estimated from the lattice component (k_L) values of a bulk sample. For consistency, the bulk sample has been prepared from the same nanoparticle ink of the thin film sample. The ink has been dried at 100°C in vacuum. The obtained nanopowders have been cold pressed (75 MPa) to from a pellet (diameter 16 mm with thickness 2 mm) which has then undergone the same thermal treatment as thin film samples. The thermoelectric properties measured for the bulk sample are presented in Figure S6a-b-d, along with those for the spin coated sample used for the calculations.

The electronic component of thermal conductivity k_e has been calculated according to the Wiedemann-Franz law ($k_e = LT\sigma$), using the Lorenz number, *L*, and electrical conductivity data. The Lorenz number L (Figure S6c) has been calculated from the Seebeck coefficient data according to Eq. 1, proposed by Kim et al. as a satisfactory approximation for semiconductors that are far from the degenerate limit[4]. L is expressed in 10^{-8} $W\Omega K^{-2}$ and α is in μV/K.

$$L = 1.5 + \exp\left(-\frac{|\alpha|}{116}\right) \quad (1)$$

Values have been verified using the more rigorous approach based on the Single Parabolic Band (SPB) model obtained by solving the Boltzmann transport equations. This method estimates L with Eq. 2, fitting the reduced chemical potential η to the experimental Seebeck coefficient with Eq. 3. $F_n(\eta)$ represents the Fermi integral, defined according to Eq. 4.

$$L = \frac{k_B^2}{e^2}\frac{3\,F_0(\eta)F_2(\eta) - 4\,F_1(\eta)^2}{F_0(\eta)^2} \quad (2)$$

$$\alpha = \frac{k_B}{e}\left(\frac{2\,F_1(\eta)}{F_0(\eta)^2} - \eta\right) \quad (3)$$

$$F_n(\eta) = \int_0^\infty \frac{x^n}{1 + \exp(x-\eta)}\,dx \quad (4)$$

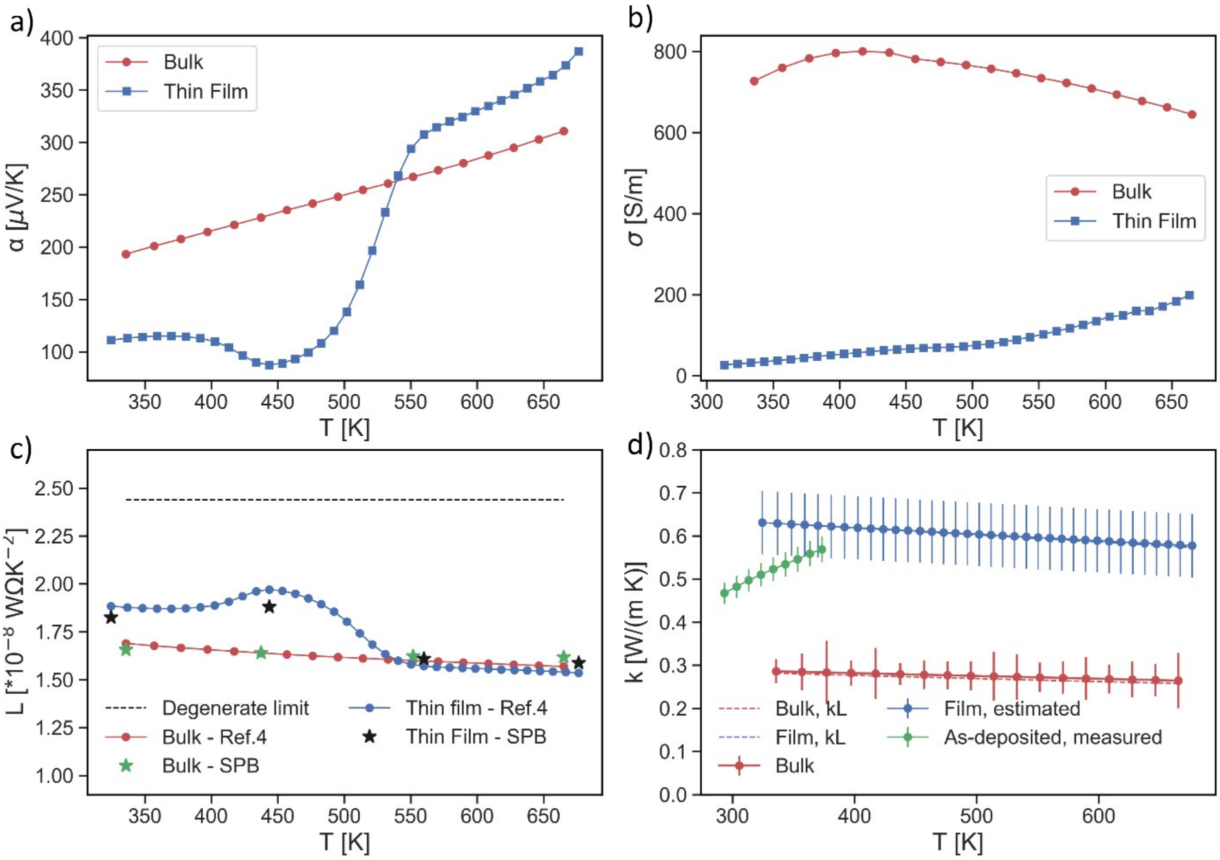

Figure S6. Thermoelectric properties for the bulk and thin film samples obtained from hot injection. a) Absolute Seebeck coefficient and b) electrical conductivity. Panel c) shows the calculations of Lorenz number based on Eq. 1 from Ref. 4 and on the Single Parabolic Band model. The degenerate limit is also shown for comparison. d) Measured thermal conductivity for the as deposited thin film sample. Thermal conductivity and lattice thermal conductivity respectively measured and estimated for the bulk and thin film sample.

Where k_B is the Boltzmann constant and e is the electronic charge.

As expected given the quite resistive nature of the samples, k_L is very close to k, indicating a low contribution of the electronic thermal conductivity. The value of k_L for the thin film sample has been corrected for the different density. The density of the bulk sample has been geometrically measured as

2.04 g/cm^3 while for the thin film sample it has been taken the cautelative value of 4.56 g/cm^3, coinciding with the full theoretical density. Measurements on the as-deposited sample gave lower values, as expected given the lack of thermal treatment, but anyway within the 20% of difference. We remark that this value of k is only an estimation, as several sample features could play a major role in determining thermal transport.

An estimate of zT can be obtained from the PF data and the calculated values of k, and is presented in Figure S7. For the slowly cooled and quenched samples the thermal conductivity is considered equal, given the small contribution of k_e to k. This estimation of zT is in accordance with literature values for pristine CZTS bulk samples[5–8]. The quenched sample presents comparatively higher values, especially in the low temperature range.

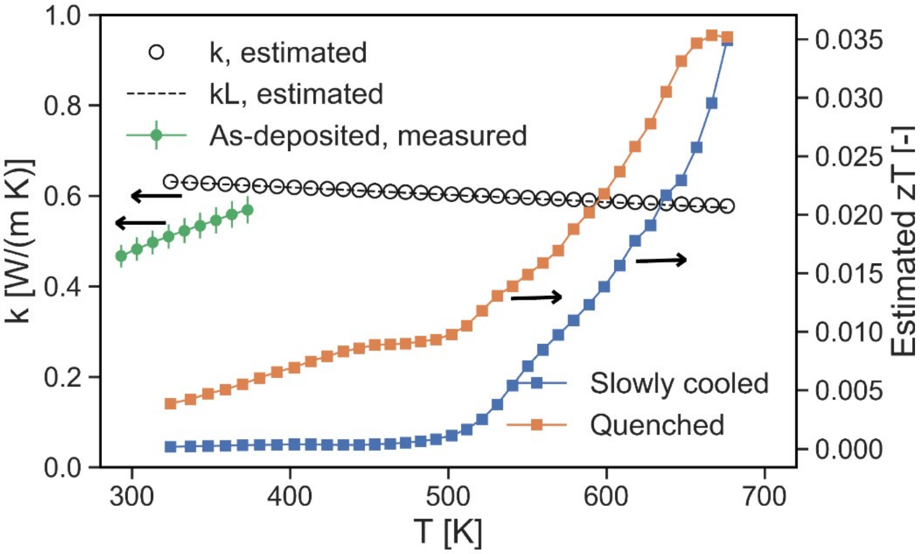

Figure S7. Measured thermal conductivity (k) for the as-deposited sample, and estimated k, with lattice component (k_L), and figure of merit zT for the thermally treated sample.

Considering the declared instrumental errors (~5%), the standard deviations of measurements (the highest is for k and is ~12%) and the differences that could be introduced by the assumptions we made in the thermal conductivity calculations, we speculate that the error on the overall zT value could be at least 30%.

Here is presented a detailed list of limitations of the approach:

1- The large porosity of the bulk sample is considered as a dilution effect which is imprecise. Indeed other factors could affect such as size and distribution of porosity, and phonon scattering from pores. For these reasons the measurement of k for the bulk sample is likely underestimated.
2- For the calculation of the thin film k, the full density is utilized. This is done to be cautelative towards the estimation of zT and to partially compensate for the effects of point 1.
3- Bulk and thin film samples are assumed having the same density-specific properties. This does not take into account the 2D dimensionality of thin films and differences in the connection and dimension of domains between bulk and thin film samples.
4- In the estimate of zT, the k of quenched and slowly-cooled samples is considered equal. For what concerns k_e this is a limited problem, as in both cases its contribution is negligible. k_L might present some differences, as disorder could help disrupting the path of phonons. Nevertheless, previously published data on similar CZTS bulk samples do not evidence major differences (<5%)[5].

Supplementary Note 7: Repeatability of electrical resistivity measurements

Figure S8 shows the complete set of electrical resistivity measurements for the sample presented in Figure 5a. Heating (shown in the main text) and cooling (added here) curves are shown in the temporal order of measurement. This data shows that the value of electrical resistivity is dominated by the thermal history of the sample, associated with disorder. It is to be stressed that, given the temporal order in which the measurements were performed, the achievement of lower-higher-lower resistivity values cannot be due to an irreversible evolution of secondary phases or sample degradation.

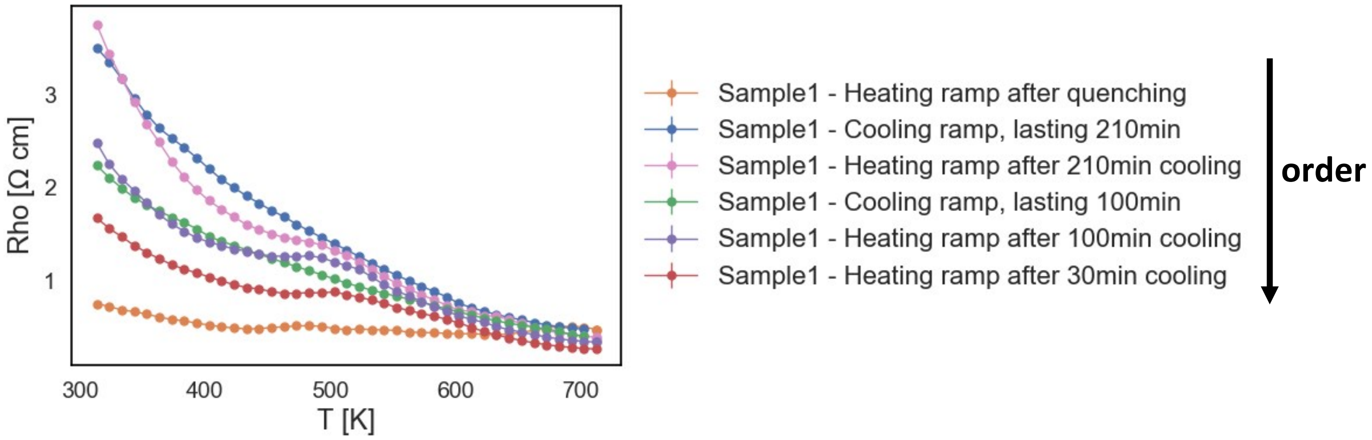

Figure S8. Full set of electrical resistivity measurements for the sample presented in Figure 5b of the main text. The temporal order of measurement is indicated in the legend.

The cooling and heating curves that are performed with corresponding cooling times (blue and pink, green and purple) show repeatability within the 7% of the initial values. This difference between the end of the cooling cycle and the beginning of the heating one shows in both cases higher values for the heating ramp. This might tentatively be associated to the extra ordering time that the sample experiences at the end of the cooling cycle (50°C → RT).

Differences along the measurement (for example between 350K and 450K for pink and blue curves) could instead be associated to the practical not perfect matching between heating and cooling ramps. Despite set to be equal, the furnace of the machine has a good control over the heating ramp but a less good one in cooling, which slightly offsets the actual heating and cooling velocities that the sample experiences. Differences are anyway in the order of some minutes.

To achieve the maximum speed of cooling of 30 min it was necessary to not perform measurements during the cooling. That is why the sample after 30min of cooling (in red) does not have an associated cooling measurement.

The Seebeck coefficient measurement of Figure 5b shows a difference of ~13% between the initial values of two successive measurements after the same cooling of 30 min (in green and orange). This difference can possibly indicate a partial retention of disorder upon repeated “fast” coolings.

References

1 U. Syafiq, N. Ataollahi, R. Di Maggio and P. Scardi, Solution-Based Synthesis and Characterization of

Cu2ZnSnS4 (CZTS) Thin Films, *Molecules*, 2019, **24**, 3454.

2 M. Leoni, T. Confente and P. Scardi, PM2K: A flexible program implementing Whole Powder Pattern Modelling, *Zeitschrift fur Krist. Suppl.*, 2006, **1**, 249–254.

3 J. J. S. Scragg, J. K. Larsen, M. Kumar, C. Persson, J. Sendler and S. Siebentritt, Cu–Zn disorder and band gap fluctuations in Cu2ZnSn(S,Se)4: Theoretical and experimental investigations, *Phys. Satus Solidi B*, 2016, **253**, 247–254.

4 H. S. Kim, Z. M. Gibbs, Y. Tang, H. Wang and G. J. Snyder, Characterization of Lorenz number with Seebeck coefficient measurement, *APL Mater.*, 2015, **3**, 1–6.

5 E. Isotta, B. Mukherjee, C. Fanciulli, N. Ataollahi, I. Sergueev, S. Stankov, R. Edla, N. M. Pugno and P. Scardi, Origin of a Simultaneous Suppression of Thermal Conductivity and Increase of Electrical Conductivity and Seebeck Coefficient in Disordered Cubic Cu2ZnSnS4, *Phys. Rev. Appl.*, 2020, **10**, 1.

6 Q. Jiang, H. Yan, Y. Lin, Y. Shen, J. Yang and M. J. Reece, Colossal thermoelectric enhancement in Cu2+xZn1−xSnS4solid solution by local disordering of crystal lattice and multi-scale defect engineering, *J. Mater. Chem. A*, 2020, **8**, 10909–10916.

7 H. Yang, L. A. Jauregui, G. Zhang, Y. P. Chen and Y. Wu, Nontoxic and abundant copper zinc tin sulfide nanocrystals for potential high-temperature thermoelectric energy harvesting, *Nano Lett.*, 2012, **12**, 540–545.

8 M. L. Liu, F. Q. Huang, L. D. Chen and I. W. Chen, A wide-band-gap p -type thermoelectric material based on quaternary chalcogenides of Cu2ZnSnQ4 (Q=S,Se), *Appl. Phys. Lett.*, 2009, **94**, 3–6.